MATERIALS CHEMISTRY FRONTIERS

RESEARCH ARTICLE

View Article Online
View Journal | View Issue

Cite this: *Mater. Chem. Front.*, 2022, **6**, 2661

A VO_3^--induced S^{2-}-exchange strategy to controllably construct a sub-nano-sulfide-functionalized layered double hydroxide for an enhanced supercapacitor performance†

Xuping Jia,[ab] Yaqi Wu,[ab] Jinyao Chi,[a] Zhenyu Xiao,*[a] Zhenhua Dang,[ab] Qi Zhang,[a] Bin Li,[a] Juan Liu*[ab] and Lei Wang*[ab]

Received 28th May 2022,
Accepted 25th July 2022

DOI: 10.1039/d2qm00503d

rsc.li/frontiers-materials

Due to the intrinsic ion channels that originate from their lamellar structure and flexible composition, layered double hydroxides (LDHs) have aroused extensive attention in the scientific community. However, the related poor conductivity and narrow interlayer spaces of LDHs limit the mass-transfer rate during the fast charging/discharging process for supercapacitor application. Here, through a VO_3^--induced S^{2-} anion-exchange process, $(Ni/Co)_{1-x}S$ sub-nanoparticle-functionalized VO_3^--doped Co/Ni-LDH hollow nanocages (S-CNV-LDH) are successfully prepared. The hierarchical hollow nanocage structure constructed by the $(Ni/Co)_{1-x}S$ sub-nanoparticle-functionalized S-CNV-LDH nanoplates can provide rich channels, abundant heterojunction interfaces and enhanced conductivity for a fast and deep mass-transfer process. Therefore, the optimized S-CNV-LDH nanocages present a high specific capacitance of 1345 F g^{-1} at 1 A g^{-1} and an excellent rate capability of 84.6% at 10 A g^{-1}. Furthermore, an S-CNV-LDH‖AC device was fabricated using active carbon (AC) as the negative electrode and a high energy density of 42.51 W h kg^{-1} is achieved at 0.8 kW kg^{-1}. This work provides a facile and controllable path for the preparation of sub-nano-sulfide *in situ* involved LDH materials.

Introduction

Supercapacitors, as a kind of energy storage device between a battery and a physical capacitor, have been widely applied in electric vehicles, portable wearable devices, rail transit, and smart grids, because they possess both the high-energy-density advantage of a battery and the high-power-density advantage of a physical capacitor.[1–8] To achieve the expected capacitance and energy density values, lots of effort has been devoted to the design and synthesis of electrode materials to satisfy the mass-transfer demand during the fast charging/discharging process.[9–14] Among reported electrode materials, layered double hydroxides (LDHs) have drawn extensive attention due to their intrinsic ion channels, which originate from their lamellar structure and flexible composition, to achieve the synergistic effect of different metal species.[15–18] However, the narrow interlayer spacing (≤1 nm) and poor conductivity of LDHs have limited the enhancement of their supercapacitor performance.[19,20] Therefore, the rational design and function of LDHs with rich channels and enhanced conductivity is necessary to satisfy the mass-transfer requirements of electrolytes and electrons for fast and deep redox reactions, which is a challenge, as well as an opportunity, in this field.[21]

Numerous effective strategies have been proposed to guide the design and function of LDH materials for an enhanced supercapacitor performance, and these can be divided into two categories.[22–24] One strategy is morphology engineering for the construction of LDH materials with various morphologies, such as nano-rods,[25–29] nano-plates,[30–32] nano-spheres[33–35] and nano-polyhedra,[36] and to build the hierarchical porous structure of mesopores and micropores in the LDH materials to create deep diffusion channels for the electrolyte. This is particularly applicable for nanomaterials with hollow structures, which can not only provide rich active centers for enhanced capacitance but also provide sufficient space to alleviate the volume effect in the charging and discharging process.[37–44] For example, the hollow $Co(VO_3)_2$–$Co(OH)_2$ composite, as reported by Zou, *et al.*, presents a higher specific

[a] *Key Laboratory of Eco-chemical Engineering, Ministry of Education, International Science and Technology Cooperation Base of Eco-chemical Engineering and Green Manufacturing, Qingdao University of Science and Technology, Qingdao 266042, P. R. China. E-mail: inorgxiaozhenyu@163.com, liujuan@qust.edu.cn, inorchemwl@126.com*

[b] *Shandong Engineering Research Center for Marine Environment Corrosion and Safety Protection, College of Environment and Safety Engineering, Qingdao University of Science and Technology, Qingdao, 266042, P. R. China*

† Electronic supplementary information (ESI) available. See DOI: https://doi.org/10.1039/d2qm00503d

capacity of 807 F g^{-1} at the current density of 1 A g^{-1}, and an excellent cycling stability in which 90% of the initial capacity is maintained after 15 000 charge–discharge cycles due to the hierarchical meso/micro-porous structure and abundant pore volume.[45] The other strategy is phase regulation, to provide more active centers and improve their conductivity *via* defect engineering, elemental doping, or the construction of heterojunctions with other highly conductive phases.[46–48] In particular, the construction of a heterojunction between LDHs and transition metal sulfides (TMSs) has been proved to be an effective means of boosting the supercapacitor capacity because TMSs possess the advantages of high intrinsic conductivity and large theoretical capacity.[49] For example, the heterojunction of the CoS_x/Ni-Co LDH, as constructed by Yang *et al.*, which provided a clear capacitance increase that was 22% higher than for the single Ni–Co LDH phase.[50] However, most of the reported TMSs in TMS–LDH heterojunctions are of a large size, which leads to sluggish ion diffusion and dead volume due to the close-packed structure of TMSs. Therefore, decreasing the size of the TMS to nano-size and even to sub-nano-size is needed for relieving the dead volume.[51] However, even synthesis methods for sub-nano-TMS-functionalized LDH materials have seldom been reported, let alone a strategy for a facile and controllable process.

Herein, we report an intelligent VO_3^--induced S^{2-} anion-exchanging strategy for the construction of $(Ni/Co)_{1-x}S$ sub-nanoparticle-functionalized VO_3^--doped Co/Ni-LDH hollow nanocages (S-CNV-LDH) at room temperature. Firstly, through a process involving Co/Ni-LDH coating and $NaVO_3$ etching, VO_3^--doped Co/Ni-LDH hollow nanocages (V-CN-LDH) are obtained using ZIF-67 as the precursor. Then, the VO_3^- anions in the V-CN-LDH will be gradually substituted by S^{2-} anions to form the $(Ni/Co)_{1-x}S$ sub-nanoparticle-functionalized V-CN-LDH (S-CNV-LDH) at room temperature, and the size of the $(Ni/Co)_{1-x}S$ sub-nanoparticles is well controlled due to the appropriate content of VO_3^- anions in V-CN-LDH. The unique hollow nanocage structure constructed using wrinkled S-CNV-LDH nanoplates and the amorphous S-CNV-LDH nanoplates functionalized with $(Ni/Co)_{1-x}S$ sub-nanoparticles can provide fast and short ion-diffusion paths and abundant active centers for enhancing the supercapacitor performance. Therefore, the optimized S-CNV-LDH nanocages present a high specific capacitance of 1345 F g^{-1} at 1 A g^{-1} and an excellent rate capability of 84.6% at 10 A g^{-1}. Furthermore, an S-CNV-LDH‖AC device is fabricated using AC as the negative electrode, and a high energy density of 42.51 W h kg^{-1} is achieved at 0.8 kW kg^{-1}.

Experimental

Chemicals

Cobalt nitrate hexahydrate [$Co(NO_3)_2{\cdot}6H_2O$; 98%, Alab (Shanghai) Chemical Technology Co., Ltd], nickel nitrate hexahydrate [$Ni(NO_3)_2{\cdot}6H_2O$; 98%, Energy Chemical], 2-methylimidazole (2-MIM, $C_4H_6N_2$; 98%, Energy Chemical), sodium sulfide nonahydrate [$Na_2S{\cdot}9H_2O$; 98.0%, Sinopharm], sodium metavanadate [$NaVO_3$; 99.5%, Energy Chemical], carbon black [Power source battery sales department], PTFE [60%, Power source battery sales department], potassium hydroxide [KOH; 85%, Energy Chemical], ethanol [C_2H_5OH; 95%, Sinopharm], and methanol [CH_3OH; 99.7%, Sinopharm] were used.

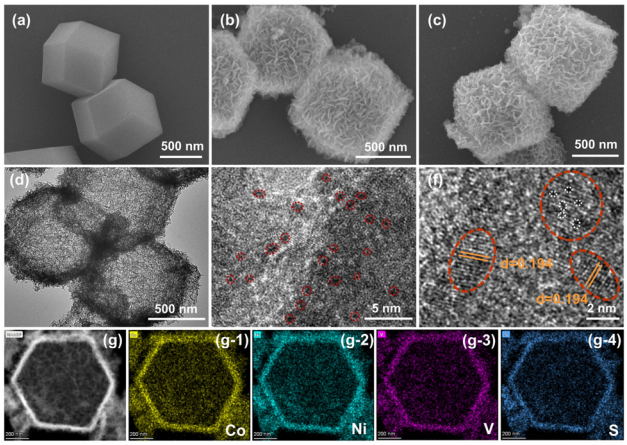

Fig. 1 SEM images of ZIF-67 (a), V-CN-LDH (b) and S-CNV-LDH (c); TEM (d) and HRTEM (e and f) images of S-CNV-LDH; and elemental mapping images (g) of Ni, Co, V and S that correspond to the S-CNV-LDH nanocages.

Synthesis of ZIF-67

In a typical procedure, $Co(NO_3)_2{\cdot}6H_2O$ (2.91 g) and 2-MIM (3.28 g) were dissolved in 250 mL methanol, respectively. Then, the 2-MIM solution was quickly poured into the cobalt nitrate solution and stirred at room temperature to form a homogeneous purple solution. After aging for 24 hours, the purple precipitate was obtained *via* centrifugation, washed several times with methanol, and dried overnight at 60 °C.

Synthesis of VO_3^--doped CoNi-LDH (V-CN-LDH)

ZIF-67 (50 mg) and $Ni(NO_3)_2{\cdot}6H_2O$ (80 mg) were dispersed in 25 mL ethanol, and the mixed suspension was stirred at room temperature for 30 min. Then, 25 mL aqueous solution containing 70 mg $NaVO_3$ was added to the suspension, and the mixture was stirred for 2 h to etch the ZIF-67 core so as to obtain the hollow VO_3^--doped CoNi-LDH nanocages (named V-CN-LDH). After that, the yellow precipitate was collected *via* centrifugation and washed several times with deionized water and ethanol. As a control, samples with different amounts of $NaVO_3$ (50 mg, 90 mg, and 110 mg) were prepared and named V-CN-LDH-50, -90, and -110, respectively.

Synthesis of S^{2-} and VO_3^- anion co-doped Co/Ni-LDH (S-CNV-LDH)

200 mg of $Na_2S{\cdot}9H_2O$ was added to the aforementioned V-CN-LDH suspension and the mixed suspension was stirred for 10 h at room temperature. After centrifugation and washing with deionized water and ethanol several times, the S-CNV-LDH sample was obtained. As a control, the amount of Na_2S was optimized, and the samples named S-CNV-LDH-100, -150, -250, and -300 were synthesized with Na_2S weights of 100 mg,

150 mg, 250 mg, and 300 mg, respectively. As a contrast, S-CV-LDH and S-CN-LDH were obtained without $Ni(NO_3)_2$ and $NaVO_3$ during the synthesis of S-CNV-LDH.

Results and discussion

According to the reported method, the ZIF-67 dodecahedron precursor with a diameter of about 800 nm (Fig. 1(a)) was synthesized using $Co(NO_3)_2$ and 2-MIM as the raw materials.[52] Then a $Ni(NO_3)_2$ and $NaVO_3$ mixed etching process was performed on the ZIF-67 precursor to construct the VO^{3-}-doped cobalt–nickel layered double hydroxide (V-CN-LDH) hollow nanocages (Fig. 1(b)). During the first $Ni(NO_3)_2$ etching step, a Co/Ni LDH shell with a thickness of 70–100 nm was formed on the surface of the ZIF-67 to obtain a ZIF-67@Co/Ni LDH egg yolk–shell structure (Fig. S1, ESI†), according to the H^+-assistant etching mechanism.[53] In the process of the etching reaction, the H^+ produced by the hydrolysis of Ni^{2+} ions can react with the 2-MIM^- anions in the ZIF-67 framework to form the free 2-HMIM *via* an acid–base reaction. The ZIF-67 core is gradually etched and free Co^{2+} is released along with more and more 2-HMIM leaving the framework.[54,55] Then, Co^{2+}, Ni^{2+} and OH^- ions in the solution may co-precipitate to form the Co/Ni LDH shell, which is deposited on the surface of ZIF-67.[56,57] The reaction equations are as follows:

$$Ni^{2+} + 2H_2O \rightarrow Ni(OH)_2 + 2H^+ \quad (1)$$

$$[Co(2\text{-}MIM)_2]_n + 2H^+ \rightarrow Co^{2+} + 2\text{-}HMIM \quad (2)$$

$$Co^{2+} + 2H_2O \rightarrow Co(OH)_2 + 2H^+ \quad (3)$$

After further mixing with $NaVO_3$ for 2 hours, the ZIF-67 core was removed to release the free Co^{2+} ions, which were further co-precipitated with enriched Ni^{2+}, VO^{3-} and OH^- on the LDH interface to form V-CN-LDH. As shown in Fig. 1(b), the V-CN-LDH presents a hierarchical structure constructed from V-CN-LDH smooth nanosheets, and the TEM image confirms its hollow structure (Fig. S1c, ESI†). Finally, the vertically arranged smooth nanosheets were transferred to wrinkled nanoplates (Fig. 1(c)) with a thickness of about 10 nm (Fig. S2, ESI†), after the Na_2S soaking process. The wrinkling phenomenon of the V-CN-LDH nanosheets may be attributed to the dimensional shrinkage effect during the anion-exchanging process between OH^- or VO^{3-} with the S^{2-} anions, because one S^{2-} anion can replace two OH^- or VO^{3-} anions. The transmission electron microscopy (TEM) image (Fig. 1(d)) further confirms the highly crimped nanosheets due to the stress of dimensional shrinkage, as well as the hollow structure of the S-CNV-LDH nanocages with a shell thickness of about 80 nm. Moreover, a lot of Ni-doped $Co_{1-x}S$ nanoparticles (Fig. 1(e)) with a sub-nanometer size of 0.58 nm (Fig. S3, ESI†) are formed and anchored on the surface of the LDH wrinkled nanoplates during the anion-exchanging process. In addition, it can be clearly seen from the EPR spectra (Fig. S4, ESI†) and Fig. 1(f) that lots of defects (g = 2.002) and lattice aberrations (Fig. 1(f)) are formed, which may provide more electrochemically active centers and fast redox kinetics for an enhanced supercapacitor performance.[58] The above anion-exchange process can be summarized using the following equations:

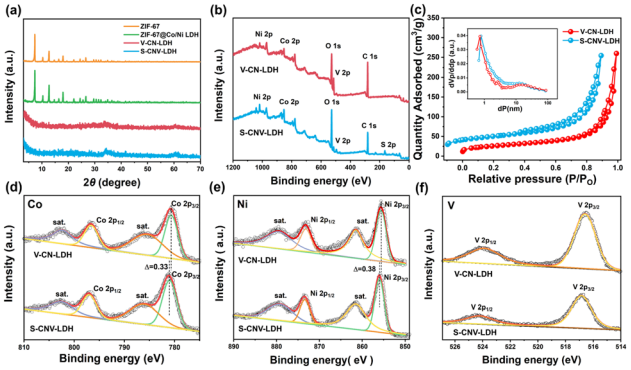

Fig. 2 (a) XRD spectra of ZIF-67, ZIF-67@LDH, V-CN-LDH and S-CNV-LDH nanocages, and (b) XPS full spectrum for the V-CN-LDH and S-CNV-LDH nanocages. (c) N_2 adsorption–desorption isotherms and (inset) pore size distribution curves; for clarity, in the main image the isotherm of S-CNV-LDH is moved up 30 $cm^3\ g^{-1}$ and shifted to the left by 0.1 P/P_0. (d)–(f) XPS spectra of the V-CN-LDH and S-CNV-LDH nanocages for Co (d), Ni (e) and V (f).

$$Co^{2+}/Ni^{2+} + 2OH^- \rightarrow Co/Ni(OH)_2 \quad (4)$$

$$Co/Ni(OH)_2 + 2VO_3^- \rightarrow Co/Ni(VO_3)_2 + 2OH^- \quad (5)$$

$$Co/Ni(VO_3)_2 + S^{2-} \rightarrow Co/NiS + 2VO_3^- \quad (6)$$

The HRTEM images reveal the existence of sub-nano crystals as minor components and the amorphous phase between the amorphous nano-domains as the major component. The lattice figure of the sub-nano crystals shows a lattice distance of 0.194 nm, which corresponds well with the (102) crystal plane of $(Ni/Co)_{1-x}S$. Moreover, the elemental mapping (Fig. 1(g)) images show that the Co, Ni, V and S elements are uniformly distributed in S-CNV-LDH, which implies that the VO_3^- and S^{2-} anions are uniformly included in the hollow nanocages. The unique defect-abundant phase and hierarchical structure can greatly increase the specific surface area and porosity, and provide sufficient ion-migration space for a higher specific capacitance, rate performance and cycling stability.

In order to track the etching and anion-exchange process and explore the phase and crystallinity of the as-prepared samples, XRD and XPS tests were employed. As shown in Fig. 2(a), the diffraction pattern of ZIF-67 is consistent with previous reports, indicating that the ZIF-67 precursor had been successfully prepared.[50] After the $Ni(NO_3)_2$ etching process, the characteristic peaks of ZIF-67 are also present, indicating that the framework of the ZIF-67 core in the ZIF-67@Co/Ni LDH core–shell structure (Fig. S1a and b, ESI†) is well maintained. After $NaVO_3$ etching, the peaks of ZIF-67 disappeared, which is consistent with the TEM result (Fig. S1c, ESI†) that the ZIF-67 core is completely removed. Due to the competitive coordination between OH^- and VO_3^- anions during the co-precipitation process, no obvious diffraction peaks are observed, corresponding to the formation of an amorphous phase. After soaking in Na_2S solution at room temperature, S-CNV-LDH presents an

amorphous phase and no sulfide diffraction peaks appear in the patterns, which corresponds well with the TEM results of sub-nanometer $(Ni/Co)_{1-x}S$. XPS analysis was performed on the V-CN-LDH and S-CNV-LDH samples to investigate the effects of S^{2-} substitution on the elemental valence state and chemical composition of the samples, as shown in Fig. 2(b)–(f). The appearance of the peaks for V and S in V-CN-LDH and S-CNV-LDH indicates that V and S had successfully been introduced into the materials *via* $NaVO_3$ etching and the S^{2-} anion-exchange process. Compared with V-CN-LDH, the peak intensity of V clearly decreased after the S^{2-} anion-exchange process, and the elemental ratio of Co : Ni : V : S changes from 11 : 9 : 5 : 0 (V-CN-LDH) to 11 : 9 : 3 : 3 (S-CNV-LDH), as shown in Table S1 (ESI†), which implies that the anion-exchange process takes place mostly between VO_3^- and S^{2-} anions. As shown in Fig. 2(d), the main peaks of the Co 2p spectrum of the S-CNV-LDH nanocages located at 781.00 eV and 797.05 eV correspond to the Co $2p_{1/2}$ and Co $2p_{3/2}$ signals, demonstrating the presence of Co^{2+}, and for the Ni 2p spectra of the S-CNV-LDH nanocages (Fig. 2(e)), the fitting peaks at 873.45 eV and 856.00 eV are attributed to Ni^{2+}. Two peaks of the V 2p orbital at a binding energy of 524.25 eV and 516.85 eV show a good fit with $2p_{1/2}$ and $2p_{3/2}$ of V^{5+} (Fig. 2(f)), which indicates that V is present through formation of the VO_3^- anion. In the S 2p spectrum of the S-CNV-LDH nanocages (Fig. S5a, ESI†), the peak located at 163.05 eV can be ascribed to the M–S chemical bond, while the binding energy at 168.85 eV is a typical peak of SO_x that originates from adsorbed oxygen on the sample surface.[59] Compared with the V-CN-LDH sample, the binding energy values of the strongest peak for Co and Ni in the S-CNV-LDH nanocages are increased by about 0.33 eV and 0.38 eV, respectively, which may be beneficial for the fast redox process of Co and Ni during the charging/discharging process. In the TGA (thermogravimetric analysis) curves (Fig. S6, ESI†), three obvious weight-loss steps can be observed. The first weight loss appears at 40–220 °C, which can be attributed to the removal of adsorbed water and crystal water in the sample. Then the dehydration reaction of OH^- ions occurs between 220 and 350 °C and a weight loss of 9.02% is achieved, which is below the normal values of reported LDH materials because some of the OH^- anions are substituted by VO_3^- and S^{2-}. The final weight loss at 350–600 °C may be attributed to pyrolyzation of the organic ligands involved.

In addition, N_2 adsorption and desorption measurements (77 K) were performed to study the surface area and pore structure of the as-prepared materials. Compared with the V-CN-LDH nanocages, the adsorption quantity of the S-CNV-LDH nanocages shows a slight decrease of about 50 $cm^3\ g^{-1}$, but the hysteresis loop for the 0.8–1.0 (P/P_0) range is significantly enhanced, indicating the increase in mesopores, which is consisted to be due to the formation of $(Ni/Co)_{1-x}S$ microcrystals and the crimping of the S-CNV-LDH nanosheets. The BJH (Barrett–Joyner–Halenda) pore size distribution further confirms the increase in the number of mesopores, which is beneficial for the fast diffusion of electrolytes. Furthermore, as shown in Fig. 2(c), the S-CNV-LDH nanocages present a larger specific surface area of 96.4 $m^2\ g^{-1}$ compared with the

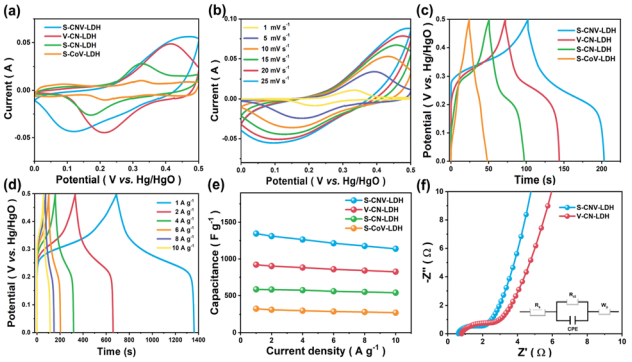

Fig. 3 CV curves of (a) S-CNV-LDH, V-CN-LDH, S-CN-LDH and S/V-CO nanocages at 10 mV s^{-1}, and (b) S-CNV-LDH nanocages at different scan rates; GCD curves of (c) S-CNV-LDH, V-CN-LDH, S-CN-LDH and S/V-CO nanocages at 6 A g^{-1}, and (d) S-CNV-LDH nanocages at different current densities; (e) specific capacitance values of S-CNV-LDH, V-CN-LDH, S-CN-LDH and S-COV nanocages at different current densities; and (f) Nyquist plots of S-CNV-LDH and V-CN-LDH nanocages.

V-CN-LDH nanocages (90.2 $m^2\ g^{-1}$) and most reported LDH and sulfide nanomaterials.[60,61]

In order to investigate the electrochemical performance of the as-prepared materials, a three-electrode test was employed using Hg/HgO as the reference electrode and a platinum as the counter electrode in 6 M KOH aqueous electrolyte. The CV and GCD curves of S-CNV-LDH, V-CN-LDH (without the S^{2-} ion-exchange process), S-CN-LDH (without the $NaVO_3$ etching process), and S-CoV-LDH (without the $Ni(NO_3)_2$ etching process) are shown in Fig. 3(a). It can be seen that these materials display obvious redox peaks in the CV curve, indicating typical pseudocapacitance characteristics, and the CV area of the S-CNV-LDH nanocages is significantly larger than that of other materials, suggesting a higher specific capacitance. In particular, the redox peak position of the CV curves (Fig. 3(b)) for the S-CNV-LDH nanocages shifted with an increase in the sweep speed, but the shape is well maintained, indicating that the S-CNV-LDH nanocages show good reversibility and a good rate performance. According to the CV curve and Formula (1) in the ESI,† the charge-storage mechanism of S-CNV-LDH was further analyzed, which shows that the modification process is jointly affected by diffusion control and surface control. In particular, with the increase in the scan rate, the capacitance contribution of surface control gradually increases, from 49.2% to 94.6%, which means that surface control plays a decisive role at a high scan speed (Fig. S7, ESI†). The GCD curves (Fig. 3(c) and (d)) of the S-CNV-LDH nanocages show excellent symmetry, corresponding to a high Coulombic efficiency of 99.8%. At the same time, the GCD curves (Fig. 3(c)) of the four samples confirm that S-CNV-LDH possesses the highest specific capacitance of 1345 F g^{-1} at the current density of 1 A g^{-1} compared with V-CN-LDH (921.6 F g^{-1}), S-CN-LDH (585 F g^{-1}) and S-CoV-LDH (325.8 F g^{-1}) (Fig. 3(e)) calculated using Formula (2) in the ESI.† In addition, S-CNV-LDH shows an excellent rate performance, maintaining 84.6% of its initial capacity as the current density is increased ten-fold. After soaking in sodium sulfide, the properties of the S-CNV-LDH material were improved to a certain extent. The main

reasons are as follows: (1) $(Ni/Co)_{1-x}S$ nanoparticles are formed on the surface of the material to enhance the conductivity of the material; (2) compared with V-CN-LDH, the BET specific surface area of S-CNV-LDH (96.4 m^2 g^{-1}) is larger than V-CN-LDH (90.2 m^2 g^{-1}), which provides more active sites for redox reactions; and (3) the pore diameter of the S-CNV-LDH material also enlarged (Fig. 2(c)), which is convenient for the mass transfer of electrolyte ions. As shown in Fig. 3(f), compared with the V-CN-LDH nanocages, the S-CNV-LDH nanocage electrode material displays a larger slope in the high-frequency region, indicating an improved ion-transfer rate, which is consistent with the increased number of mesopores. By fitting with the equivalent circuit shown in the inset to Fig. 3(f), it is proved that S-CNV-LDH has a smaller R_s (0.571 Ω) and R_{ct} (0.877 Ω) than V-CN-LDH (R_s = 0.571 Ω, R_{ct} = 0.877 Ω), as shown in Table S2 (ESI†).

To improve the supercapacitor performance of the as-prepared materials, the amounts of $NaVO_3$ and Na_2S were optimized and their CV and GCD curves are shown in Fig. S8 and S9 (ESI†). For the LDH samples prepared using different amounts of $NaVO_3$, for the increase in the $NaVO_3$ content, the specific capacitance of V-CN-LDH increased initially and then decreased due to the difference in the thickness of their nanosheet units (Fig. S11, ESI†). The related capacitance values of V-CN-LDH-50/-70/-90/-100 were 826.0, 921.6, 848.2, and 820.8 F g^{-1}, respectively at the current density of 1 A g^{-1} (Fig. S10a, ESI†). V-CN-LDH-70 presents the maximum specific capacity, and was selected for the subsequent S^{2-} substitution process. For the samples synthesized with different Na_2S contents, their specific capacitances also display a normal distribution. With an increase in the Na_2S content from 100 mg to 200 mg, the S-CNV-LDH-100, S-CNV-LDH-150 and S-CNV-LDH present specific capacity values of 952.8, 1234.6 and 1344.6 F g^{-1} at 1 A g^{-1} (Fig. S10b, ESI†), which may be attributed to the increased amount of S. With a further increase in the Na_2S content, the specific capacity values of S-CNV-LDH-250 and S-CNV-LDH-300 gradually decreased due to the collapse of the hollow nanocage structure (Fig. S12, ESI†).

In order to further test the practical application of the material, an S-CNV-LDH‖AC asymmetric supercapacitor (ACS) device was assembled using S-CNV-LDH as the positive electrode and AC as the negative electrode in a 6 M KOH electrolyte solution. The CV curve and GCD curve of the negative AC are shown in Fig. S13 (ESI†) with a capacity of 272.3 F g^{-1} at the current density of 1 A g^{-1}. According to Formula (3) in the ESI,† the positive and negative electrodes are matched with the optimal mass ratio of 1 : 2.5 from the CV curve at 10 mV s^{-1} (Fig. 4(a)). The CV curves for different voltage ranges are displayed in Fig. S14a (ESI†), and it can be seen that the oxygen evolution reaction will occur at a high voltage. Therefore, the voltage range of 0–1.6 V was selected for the subsequent energy-storage process. As shown in (Fig. 4(b)), the CV curves of the S-CNV-LDH‖AC ACS device show similar shapes at scan rates from 1 to 100 mV s^{-1}, indicating an excellent rate performance and reaction kinetics. According to the GCD curves (Fig. 4(c)), the specific capacitances of the S-CNV-LDH‖AC ACS at different current densities (1, 2, 4, 6, 8 and 10 A g^{-1}) are 119.6, 110.1, 101.8, 96.75, 93.0 and 90.0 F g^{-1}, respectively (Fig. S14b, ESI†). The Ragone plot of energy density *versus* power density was calculated according to Formula (4) and (5). As shown in Fig. 4(d), a high energy density of 42.5 W h kg^{-1} is achieved at the power density of 0.8 kW kg^{-1}, and an energy density of 32 W h kg^{-1} is maintained even at a high power density of 8 kW kg^{-1}, which is significantly higher than other supercapacitor devices assembled using transition metal sulfide/hydroxide/vanadate nanomaterials and AC, as shown in Table S3 (ESI†).[61–74]

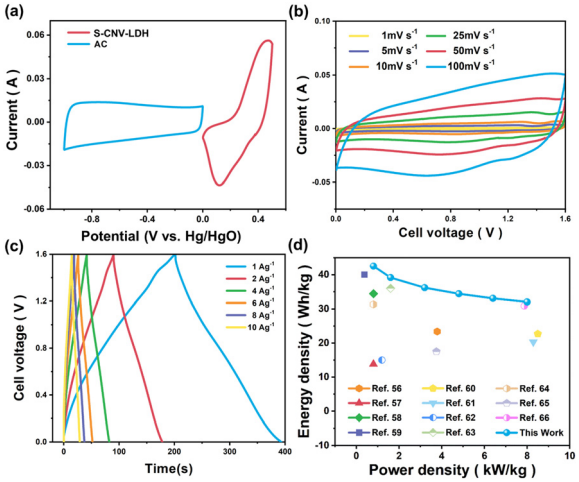

Fig. 4 (a) CV curves of S-CNV-LDH nanocage (load mass, 2 mg) and AC (load mass, 5 mg) electrodes at 10 mV s^{-1}. (b) CV curves at different scan rates, and (c) GCD curves in different current densities of the S-CNV-LDH‖AC. (d) Ragone plot of the S-CNV-LDH‖AC device and comparison with other supercapacitors.

In addition, the S-CNV-LDH‖AC ASC device shows an excellent lifespan and maintains 62.64% of its initial capacity after 10 000 cycles (Fig. 5(a)). It is worth noting that the capacity of the S-CNV-LDH‖AC ASC in the first 100 cycles decreases significantly, which may be due to VO_3^- dissolution (Fig. S15, ESI†). In practical applications, the ASC device can make an electronic thermometer work for 20 min (Fig. 5(b)) when

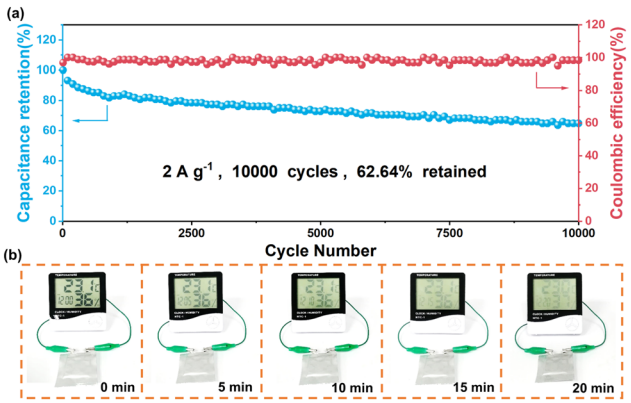

Fig. 5 (a) Cycling stability and Coulombic efficiency of the S-CNV-LDH‖AC device; and (b) one soft-packaged battery of 3 × 3 cm used to power a thermometer for 20 min.

charging for 17 s (Fig. S16, ESI†), which presents a great application significance.

Conclusions

Herein, $(Ni/Co)_{1-x}S$ sub-nanoparticle-functionalized VO_3^--doped Co/Ni-LDH hollow nanocages (S-CNV-LDH) were successfully constructed using a VO_3^--induced S^{2-} anion-exchange process. The anion-exchange process mainly occurs between S^{2-} and VO_3^-, and the involved VO_3^- anions with a suitable content will effectively limit the size of $(Ni/Co)_{1-x}S$ to the sub-nano level. The unique hollow structure constructed *via* self-supported wrinkled nanoplates and a large amount of embedded $(Ni/Co)_{1-x}S$ sub-nanoparticles in the S-CNV-LDH nanoplates can provide rich channels and an accessible interface for an enhanced supercapacitor performance. Therefore, S-CNV-LDH presents a high capacitance of 1345 F g^{-1} at 1 A g^{-1} and an outstanding rate capability, maintaining 84.6% of the initial capacity as the current density is increased ten-fold. Furthermore, an S-CNV-LDH‖AC hybrid supercapacitor was fabricated, which shows a high energy density of 42.5 W h kg^{-1} when the energy density is 0. 8 kW kg^{-1}. This work provides a facile and controllable means of constructing sub-nano-sulfide-functionalized LDH materials for energy-storage and energy-conversion applications.

Author contributions

Xuping Jia: investigation, experimental analysis, and writing the original draft. Yaqi Wu: methodology, experimental analysis. Jinyao Chi: experimental analysis. Zhenyu Xiao: conceptualization, writing and funding acquisition. Zhenhua Dang: project administration. Qi Zhang: experimental analysis. Bin Li: data curation. Juan Liu: writing, data curation and funding acquisition. Lei Wang: funding acquisition.

Conflicts of interest

The authors declare that there is no conflict of interest.

Acknowledgements

This work was supported by the National Natural Science Foundation of China (52072197, 21805155, and 21971132), the Outstanding Youth Foundation of Shandong Province, China (ZR2019JQ14), the Youth Innovation and Technology Foundation of Shandong Higher Education Institutions, China (2019KJC004), the Natural Science Foundation of Shandong Province, China (ZR2019MEM023, and ZR2019MB042), the Major Scientific and Technological Innovation Project (2019JZZY020405), the Taishan Scholar Young Talent Program (tsqn201909114), and the Major Basic Research Program of the Natural Science Foundation of Shandong Province under Grant (ZR2020ZD09).

Notes and references

1 B. Xu, H. Zhang, H. Mei and D. Sun, Recent progress in metal–organic framework-based supercapacitor electrode materials, *Coord. Chem. Rev.*, 2020, **420**, 213438.
2 L. Yang, X. Guo, Z. Jin, W. Guo, G. Duan, X. Liu and Y. Li, Emergence of melanin-inspired supercapacitors, *Nano Today*, 2021, **37**, 101075.
3 F. Boorboor Ajdari, E. Kowsari, M. Niknam Shahrak, A. Ehsani, Z. Kiaei, H. Torkzaban, M. Ershadi, S. Kholghi Eshkalak, V. Haddadi-Asl, A. Chinnappan and S. Ramakrishna, A review on the field patents and recent developments over the application of metal organic frameworks (MOFs) in supercapacitors, *Coord. Chem. Rev.*, 2020, **422**, 213441.
4 N. Raza, T. Kumar, V. Singh and K. Kim, Recent advances in bimetallic metal–organic framework as a potential candidate for supercapacitor electrode material, *Coord. Chem. Rev.*, 2021, **430**, 213660.
5 S. Li, J. Lin, W. Xiong, X. Guo, D. Wu, Q. Zhang, Q. Zhu and L. Zhang, Design principles and direct applications of cobalt-based metal–organic frameworks for electrochemical energy storage, *Coord. Chem. Rev.*, 2021, **438**, 213872.
6 S. Bi, H. Banda, M. Chen, L. Niu, M. Chen, T. Wu, J. Wang, R. Wang, J. Feng, T. Chen, M. Dincă, A. A. Kornyshev and G. Feng, Molecular understanding of charge storage and charging dynamics in supercapacitors with MOF electrodes and ionic liquid electrolytes, *Nat. Mater.*, 2020, **19**, 552–558.
7 Q. Li, Z. Dai, J. Wu, W. Liu, T. Di, R. Jiang, X. Zheng, W. Wang, X. Ji, P. Li, Z. Xu, X. Qu, Z. Xu and J. Zhou, Fabrication of ordered macro-microporous single-crystalline MOF and its derivative carbon material for supercapacitor, *Adv. Energy Mater.*, 2020, **10**, 1903750.
8 C. Chen, C. Zhao, C. Li, J. Liu and D. Gui, Porous $NiCo_2O_4$ nanowire arrays as supercapacitor electrode materials with extremely high cycling Stability, *Chem. Res. Chin. Univ.*, 2020, **36**, 715–720.
9 Y. Zhou, H. Qi, J. Yang, Z. Bo, F. Huang, M. S. Islam, X. Lu, L. Dai, R. Amal and C. H. Wang, Two-birds-one-stone: Multifunctional supercapacitors beyond traditional energy storage, *Energy Environ. Sci.*, 2021, **14**, 1854–1896.
10 T. Yi, J. Pan, T. Wei, Y. Li and G. Cao, $NiCo_2S_4$-based nanocomposites for energy storage in supercapacitors and batteries, *Nano Today*, 2020, **33**, 100894.
11 G. Xiang, Y. Meng, G. Qu, J. Yin, B. Teng, Q. Wei and X. Xu, Dual-functional $NiCo_2S_4$ polyhedral architecture with superior electrochemical performance for supercapacitors and lithium-ion batteries, *Sci. Bull.*, 2020, **65**, 443–451.
12 Q. Wang, F. Gao, B. Xu, F. Cai, F. Zhan, F. Gao and Q. Wang, ZIF-67 derived amorphous $CoNi_2S_4$ nanocages with nanosheet arrays on the shell for a high-performance asymmetric supercapacitor, *Chem. Eng. J.*, 2017, **327**, 387–396.
13 W. Liu, F. Zhu, B. Ge, L. Sun, Y. Liu and W. Shi, MOF derived ZnO/C@(Ni,Co)Se_2 core–shell nanostructure on carbon cloth for high-performance supercapacitors, *Chem. Eng. J.*, 2022, **427**, 130788.

14 Y. Yan, A. Li, C. Lu, T. Zhai, S. Lu, W. Li and W. Zhou, Double-layered yolk–shell microspheres with $NiCo_2S_4$–Ni_9S_8–C hetero-interfaces as advanced battery-type electrode for hybrid supercapacitors, *Chem. Eng. J.*, 2020, **396**, 125316.
15 F. Chen, C. Chen, Q. Hu, B. Xiang, T. Song, X. Zou, W. Li, B. Xiong and M. Deng, Synthesis of CuO@CoNi LDH on Cu foam for high-performance supercapacitors, *Chem. Eng. J.*, 2020, **401**, 126145.
16 T. Liu, H. Zhou, G. Zhong, X. Yan, X. Su and Z. Lin, Synthesis of NiFeAl LDHs from electroplating sludge and their excellent supercapacitor performance, *J. Hazard. Mater.*, 2021, **404**, 124113.
17 X. Han, J. Li, J. Lu, S. Luo, J. Wan, B. Li, C. Hu and X. Cheng, High mass-loading NiCo-LDH nanosheet arrays grown on carbon cloth by electrodeposition for excellent electrochemical energy storage, *Nano Energy*, 2021, **86**, 106079.
18 G. Huang, Y. Li, R. Chen, Z. Xiao, S. Du, Y. Huang, C. Xie, C. Dong, H. Yi and S. Wang, Electrochemically formed PtFeNi alloy nanoparticles on defective NiFe LDHs with charge transfer for efficient water splitting, *Chin. J. Catal.*, 2022, **43**, 1101–1110.
19 B. Ramulu, S. Chandra Sekhar, S. J. Arbaz and J. S. Yu, Nano-Ag laminated ternary layered double hydroxides for hybrid supercapacitors, *Chem. Eng. J.*, 2021, **420**, 130376.
20 J. Ma, J. Xia, Z. Liang, X. Chen, Y. Du and C. Yan, Layered double hydroxide hollowcages with adjustable layer spacing for high performance hybrid supercapacitor, *Small*, 2021, **17**, 2104423.
21 N. Jayababu and D. Kim, CuCo LDHs coated CuCoTe honeycomb-like nanosheets as a novel anode material for hybrid supercapacitors, *Small*, 2021, **17**, 2102369.
22 X. Gao, P. Wang, Z. Pan, J. P. Claverie and J. Wang, Recent progress in two-dimensional layered double hydroxides and their derivatives for supercapacitors, *ChemSusChem*, 2020, **13**, 1226–1254.
23 C. Jing, B. Dong and Y. Zhang, Chemical modifications of layered double hydroxides in the supercapacitor, *Energy Environ. Mater.*, 2020, **3**, 346–379.
24 G. M. Tomboc, J. Kim, Y. Wang, Y. Son, J. Li, J. Y. Kim and K. Lee, Hybrid layered double hydroxides as multifunctional nanomaterials for overall water splitting and supercapacitor applications, *J. Mater. Chem. A*, 2021, **9**, 4528–4557.
25 S. J. Patil, N. R. Chodankar, R. B. Pujari, Y. K. Han and D. W. Lee, Core–shell hetero-nanostructured 1D transition metal polyphosphates decorated 2D bimetallic layered double hydroxide for sustainable hybrid supercapacitor, *J. Power Sources*, 2020, **466**, 228286.
26 T. Yang, J. Ye, S. Chen, S. Liao, H. Chen, L. Yang, X. Xu and F. Wang, Construction of nanowall-supported-nanorod nico ldh array electrode with high mass-loading on carbon cloth for high-performance asymmetric supercapacitors, *Electrochim. Acta*, 2020, **362**, 137081.
27 C. Lu, Y. Yan, T. Zhai, Y. Fan and W. Zhou, 2 nm-thick NiCo LDH@NiSe single-crystal nanorods grown on Ni Foam as integrated electrode with enhanced areal capacity for supercapacitors, *Batteries Supercaps*, 2020, **3**, 534–540.
28 Y. He, X. Zhang, J. Wang, Y. Sui, J. Qi, Z. Chen, P. Zhang, C. Chen and W. Liu, Constructing Co(OH)F nanorods@-NiCo-LDH nanocages derived from ZIF-67 for high-performance supercapacitors, *Adv. Mater. Interfaces*, 2021, **8**, 2100642.
29 K. Zheng, L. Liao, Y. Zhang, H. Tan, J. Liu, C. Li and D. Jia, Hierarchical NiCo-LDH core/shell homostructural electrodes with MOF-derived shell for electrochemical energy storage, *J. Colloid Interface Sci.*, 2022, **619**, 75–83.
30 Y. Zhang, D. F. Du, X. J. Li, H. M. Sun, L. Lo, P. Bai, W. Xing, Q. Z. Xue and Z. F. Yan, Electrostatic self-assembly of sandwich-like CoAl-LDH/polypyrrole/graphene nanocomposites with enhanced capacitive performance, *ACS Appl. Mater. Interfaces*, 2017, **9**, 31699–31709.
31 W. Hu, L. Chen, X. Wu, M. Du, Y. Song, Z. Wu and Q. Zheng, Slight zinc doping by an ultrafast electrodeposition process boosts the cycling performance of layered double hydroxides for ultralong-life-span supercapacitors, *ACS Appl. Mater. Interfaces*, 2021, **13**, 38346–38357.
32 Q. Yin, D. Li, J. Zhang, Y. Zhao, J. Luo, M. Shao and J. Han, An all-solid-state fiber-type supercapacitor based on hierarchical Ni/NiO@CoNi-layered double hydroxide core–shell nanoarrays, *J. Alloys Compd.*, 2020, **813**, 152187.
33 N. Zhao, Y. Feng, H. Zhao, H. Fan, S. Tian and B. Hu, Simple electrodeposition of 3D NiCoFe-layered double hydroxide nanosheet assembled nanospheres/nanoflowers on carbon cloth for high performance hybrid supercapacitors, *J. Alloys Compd.*, 2022, **901**, 163566.
34 P. Li, X. Liu, M. Arif, H. Yan, C. Hu, S. Chen and X. Liu, In situ growth of glucose-intercalated LDHs on $NiCo_2S_4$ hollow nanospheres to enhance energy storage capacity for hybrid supercapacitors, *Colloids Surf., A*, 2022, **644**, 128823.
35 J. Tian, A. Zhang, R. Liu, W. Huang, Z. Yuan, R. Zheng, D. Wei and L. Jingquan, Preparation of CoS_2 supported flower-like NiFe layered double hydroxides nanospheres for high-performance supercapacitors, *J. Colloid Interface Sci.*, 2020, **579**, 607–618.
36 L. Kumar, P. K. Boruah, S. Borthakur, L. Saikia, M. R. Das and S. Deka, CuCo-layered double hydroxide nanosheet-based polyhedrons for flexible supercapacitor cells, *ACS Appl. Nano Mater.*, 2021, **4**, 5250–5262.
37 L. Wang, J. Wan, Y. Zhao, N. Yang and D. Wang, Hollow multi-shelled structures of Co_3O_4 dodecahedron with unique crystal orientation for enhanced photocatalytic CO_2 reduction, *J. Am. Chem. Soc.*, 2019, **141**, 2238–2241.
38 C. Wang, L. Zhang, M. Al Mamun, Y. Dou, P. Liu, D. Su, G. Wang, S. Zhang, D. Wang and H. Zhao, A hollow-shell structured V_2O_5 electrode-based symmetric full Li-ion battery with highest capacity, *Adv. Energy Mater.*, 2019, **9**, 1900909.
39 D. Mao, J. Wan, J. Wang and D. Wang, Sequential templating approach: A groundbreaking strategy to create hollow multishelled structures, *Adv. Mater.*, 2018, **31**, 1802874.
40 C. Jiao, Z. Wang, X. Zhao, H. Wang, J. Wang, R. Yu and D. Wang, Triple-shelled manganese–cobalt oxide hollow

dodecahedra with highly enhanced performance for rechargeable alkaline batteries, *Angew. Chem., Int. Ed.*, 2019, **58**, 996–1001.

41 E. H. M. Salhabi, J. Zhao, J. Wang, M. Yang, B. Wang and D. Wang, Hollow multi-shelled structural TiO_{2-x} with multiple spatial confinement for long-life lithium–sulfur batteries, *Angew. Chem., Int. Ed.*, 2019, **58**, 9078–9082.

42 J. Wang, H. Tang, L. Zhang, H. Ren, R. Yu, Q. Jin, J. Qi, D. Mao, M. Yang, Y. Wang, P. Liu, Y. Zhang, Y. Wen, L. Gu, G. Ma, Z. Su, Z. Tang, H. Zhao and D. Wang, Multi-shelled metal oxides prepared *via* an anion-adsorption mechanism for lithium-ion batteries, *Nat. Energy*, 2016, **1**, 16050.

43 J. Wang, H. Tang, H. Ren, R. Yu, J. Qi, D. Mao, H. Zhao and D. Wang, pH-regulated synthesis of multi-shelled manganese oxide hollow microspheres as supercapacitor electrodes using carbonaceous microspheres as templates, *Adv. Sci.*, 2014, **1**, 1400011.

44 J. Qi, X. Lai, J. Wang, H. Tang, H. Ren, Y. Yang, Q. Jin, L. Zhang, R. Yu, G. Ma, Z. Su, H. Zhao and D. Wang, Multi-shelled hollow micro-/nanostructures, *Chem. Soc. Rev.*, 2015, **44**, 4749–6773.

45 Y. Zhang, H. Chen, C. Guan, Y. Wu, C. Yang, Z. Shen and Q. Zou, Energy-saving synthesis of MOF-derived hierarchical and hollow $Co(VO_3)_2$–$Co(OH)_2$ composite leaf arrays for supercapacitor electrode materials, *ACS Appl. Mater. Interfaces*, 2018, **10**, 18440–18444.

46 X. Chu, F. Meng, H. Yang, W. Zhang, T. Qin, Z. Wang, S. Molin, P. Jasinski and W. Zheng, Cu-doped layered double hydroxide constructs the performance-enhanced supercapacitor *via* band gap reduction and defect triggering, *ACS Appl. Energy Mater.*, 2022, **5**, 2192–2201.

47 M. M. Aya, R. Mohamed and K. A. Nageh, Recent advances on zeolitic imidazolate -67 metal–organic framework-derived electrode materials for electrochemical supercapacitors, *J. Energy Storage*, 2020, **34**, 102195.

48 B. Hou, L. Ma, X. Zang, N. Shang, J. Song, X. Zhao, C. Wang, J. Qi, J. Wang and R. Yu, Design and construction of 3D porous $Na_3V_2(PO_4)_3$/C as high performance cathode for sodium ion batteries, *Chem. Res. Chin. Univ.*, 2021, **37**, 265–273.

49 W. Jeon, H. K. Chang, W. Jae-Hyung, H. K. Ji, A. K. Yoong and Y. Cheol-Min, Sulfur-doping effects on the supercapacitive behavior of porous spherical graphene electrode derived from layered double hydroxide template, *Appl. Surf. Sci.*, 2021, **558**, 149867.

50 X. Guan, M. Huang, L. Yang, G. Wang and X. Guan, Facial design and synthesis of CoS_x/Ni–Co LDH nanocages with rhombic dodecahedral structure for high-performance asymmetric supercapacitors, *Chem. Eng. J.*, 2019, **372**, 151–162.

51 P. Prabhu, V. Jose and J. Lee, Design strategies for development of TMD-based heterostructures in electrochemical energy systems, *Matter*, 2020, **2**, 526–553.

52 Y. Bao, X. Jia, L. Liu, Z. Xiao, R. Bu, S. Lv, J. Liu, Z. Dang, Q. Zhang and L. Wang, Step-by-step etching strategy to construct multiple-shell amorphous Co/Ni-$(PO_4)_x(OH)_y$ hollow polyhedron for supercapacitor application, *J. Solid State Chem.*, 2021, **304**, 122618.

53 Z. Y. Xiao, Y. X. Bao, Z. J. Li, X. D. Huai, M. H. Wang, P. Liu and L. Wang, Construction of hollow cobalt-nickel phosphate nanocages through a controllable etching strategy for high supercapacitor performances, *ACS Appl. Energy Mater.*, 2019, **2**, 1086–1092.

54 Z. Jiang, Z. Li, Z. Qin, H. Sun, X. Jiao and D. Chen, LDH nanocages synthesized with MOF templates and their high performance as supercapacitors, *Nanoscale*, 2013, **5**, 11770–11775.

55 H. Hu, B. Guan, B. Xia and X. W. D. Lou, Designed formation of Co_3O_4/$NiCo_2O_4$ double-shelled nanocages with enhanced pseudocapacitive and electrocatalytic properties, *J. Am. Chem. Soc.*, 2015, **137**, 5590–5595.

56 P. L. He, X. Yu and X. W. D. Lou, Carbon-incorporated nickel–cobalt mixed metal phosphide nanoboxes with enhanced electrocatalytic activity for oxygen evolution, *Angew. Chem., Int. Ed.*, 2017, **56**, 3897–3900.

57 Y. Bao, Y. Deng, M. Wang, Z. Xiao, M. Wang, Y. Fu, Z. Guo, Y. Yang and L. Wang, A controllable top-down etching and in situ oxidizing strategy: Metal–organic frameworks derived α-Co/Ni$(OH)_2$@Co_3O_4 hollow nanocages for enhanced supercapacitor performance, *Appl. Surf. Sci.*, 2020, **504**, 144395.

58 R. Zheng, C. Shu, X. Chen, Y. Yan, M. He, D. Du, L. Ren, A. Hu and J. Long, Unique intermediate adsorption enabled by anion vacancies in metal sulfide embedded MXene nanosheets overcoming kinetic barriers of oxygen electrode reactions in lithium–oxygen batteries, *Energy Storage Mater.*, 2021, **40**, 41–50.

59 X. Huang, J. Tang, B. Luo, R. Knibbe, T. Lin, H. Hu, M. Rana, Y. Hu, X. Zhu, Q. Gu, D. Wang and L. Wang, Sandwich-like ultrathin TiS_2 nanosheets confined within N,S codoped porous carbon as an effective polysulfide promoter in lithium–sulfur batteries, *Adv. Energy Mater.*, 2019, **9**, 1901872.

60 J. Zou, D. Xie, J. Xu, X. Song, X. Zeng, H. Wang and F. Zhao, Rational design of honeycomb Ni-Co LDH/graphene composite for remarkable supercapacitor *via* ultrafast microwave synthesis, *Appl. Surf. Sci.*, 2022, **571**, 151322.

61 P. Cai, T. Liu, L. Zhang, B. Cheng and J. Yu, ZIF-67 derived nickel cobalt sulfide hollow cages for high-performance supercapacitors, *Appl. Surf. Sci.*, 2020, **504**, 144501.

62 X. Lv, W. Huang, Q. Shi, L. Tang and J. Tang, Synthesis of CoV_2O_6/CNTs composites *via* ultrasound as electrode materials for supercapacitors, *J. Mater. Sci.: Mater. Electron.*, 2020, **31**, 2388–2397.

63 X. Zhao, Q. Ma, K. Tao and L. Han, ZIF-derived porous $CoNi_2S_4$ on intercrosslinked polypyrrole tubes for high-performance asymmetric supercapacitors, *ACS Appl. Energy Mater.*, 2021, **4**, 4199–4207.

64 T. Liu, J. Liu, L. Zhang, B. Cheng and J. Yu, Construction of nickel cobalt sulfide nanosheet arrays on carbon cloth for performance-enhanced supercapacitor, *J. Mater. Sci. Technol.*, 2020, **47**, 113–121.

65 K. Tao, X. Han, Q. Cheng, Y. Yang, Z. Yang, Q. Ma and L. Han, A zinc cobalt sulfide nanosheet array derived from a 2D bimetallic metal–organic frameworks for high-performance supercapacitors, *Chem. – Eur. J.*, 2018, **24**, 12584–12591.

66 L. Han, X. Liu, Z. Cui, Y. Hua, C. Wang, X. Zhao and X. Liu, Hierarchical copper cobalt sulfide nanobelt arrays for high performance asymmetric supercapacitors, *Inorg. Chem. Front.*, 2021, **8**, 3025–3036.

67 A. M. Patil, A. C. Lokhande, P. A. Shinde, J. H. Kim and C. D. Lokhande, Vertically aligned NiS nano-flakes derived from hydrothermally prepared $Ni(OH)_2$ for high performance supercapacitor, *J. Energy Chem.*, 2018, **27**, 791–800.

68 Y. Fan, Y. Liu, X. Liu, Y. Liu and L. Fan, Hierarchical porous $NiCo_2S_4$-rGO composites for high-performance supercapacitors, *Electrochim. Acta*, 2017, **249**, 1–8.

69 S. Liu and S. C. Jun, Hierarchical manganese cobalt sulfide core–shell nanostructures for high-performance asymmetric supercapacitors, *J. Power Sources*, 2017, **342**, 629–637.

70 L. Hou, Y. Shi, S. Zhu, G. Pang, M. Rehan, X. Zhang and C. Yuan, Hollow mesoporous hetero-$NiCo_2S_4$/Co_9S_8 submicro-spindles: unusual formation and excellent pseudocapacitance towards hybrid supercapacitors, *J. Mater. Chem. A*, 2017, **5**, 133–144.

71 Y. Liu, G. Liu, X. Nie, A. Pan, S. Liang and T. Zhu, In situ formation of Ni_3S_2-$Cu_{1.8}S$ nanosheets to promote hybrid supercapacitor performance, *J. Mater. Chem. A*, 2019, **7**, 11044–11052.

72 W. Hu, L. Chen, M. Du, Y. Song, Z. Wu and Q. Zheng, Hierarchical NiCo-layered double hydroxide nanoscroll@PANI nanocomposite for high performance battery-type supercapacitor, *Electrochim. Acta*, 2020, **338**, 135869.

73 W. Zhang, H. Fan, Q. Liu, N. Ta, Y. Pu, X. Chen, Y. Sui, E. Wang and P. Cao, Nickel-rich NiCo LDHs supported on hollow carbon shells for hybrid supercapacitors, *Electrochim. Acta*, 2021, **395**, 139167.

74 Z. Yang, Q. Cheng, W. Li, Y. Li, C. Yang, K. Tao and L. Han, Construction of 2D ZIF-derived hierarchical and hollow NiCo-LDH ''nanosheet-on-nanosheet'' arrays on reduced graphene oxide/Ni foam for boosted electrochemical energy storage, *J. Alloys Compd.*, 2021, **850**, 156864.